

MULTI-FREQUENCY ULTRASOUND DIRECTED SELF-ASSEMBLY

Christopher Tre Presley

Thesis submitted to the faculty of the Virginia Polytechnic Institute and State University

in partial fulfillment of the requirements for the degree of

Master of Science

in

Mechanical Engineering

Bart Raeymaekers, Chair

Fernando Guevara Vasquez

Brian Lattimer

September 14, 2023

Blacksburg, Virginia

Keywords: External field directed self-assembly; ultrasound directed self-assembly;

multi-frequency wave field; engineered composite materials; manufacturing

Copyright 2023, Christopher Tre Presley

MULTI-FREQUENCY ULTRASOUND DIRECTED SELF-ASSEMBLY

Christopher Tre Presley

Abstract

Ultrasound directed self-assembly (DSA) relies on the acoustic radiation force associated with a standing ultrasound wave to organize particles dispersed in a fluid medium into specific patterns. State-of-the-art ultrasound DSA methods can only organize particles into (quasi-)periodic patterns, limited by the use of single-frequency ultrasound wave fields. Acoustic holography and acoustic waveguides provide alternatives to assembling complex patterns of particles, but generally provide low spatial accuracy and are not re-configurable because they require custom hardware for each specific pattern of particles, which is impractical. We introduce multi-frequency ultrasound wave fields to organize particles in non-periodic patterns. We theoretically derive and experimentally validate a solution methodology to determine the operating parameters (frequency, amplitude, phase) of any number and spatial arrangement of ultrasound transducers, required to assemble spherical particles dispersed in an inviscid fluid medium into any specific two-dimensional pattern. The results show that multi-frequency ultrasound DSA enables the assembly of complex, non-periodic patterns of particles with substantially fewer ultrasound transducers than single-frequency ultrasound DSA, and without incurring a penalty in terms of accuracy. The results of this work fundamentally transform the state-of-the-art knowledge of ultrasound DSA. Multi-frequency ultrasound wave fields enable a near-unlimited complexity of patterns of particles that can be assembled, increasing the relevance of the technology to practical implementation in engineering applications such as manufacturing of engineered composite materials that derive their properties from the

spatial organization of the filler in the matrix material. Although this work focuses specifically on ultrasound wave fields, the theoretical model is valid for all wave phenomena.

MULTI-FREQUENCY ULTRASOUND DIRECTED SELF-ASSEMBLY

Christopher Tre Presley

General Audience Abstract

Ultrasound directed self-assembly (DSA) is the process where particles dispersed in a fluid medium assemble into specific patterns due to their interactions with a sound wave and/or other particles. Current ultrasound DSA methods use a single-frequency ultrasound wave to assemble particles into specific patterns, which creates repeating patterns within the fluid medium. Other methods of assembling particles that allow for more complex, non-repeating patterns generally provide low spatial accuracy and do not allow dynamically changing the pattern as they require custom hardware for each specific pattern of particles, rendering these methods impractical. We use many ultrasound waves each with a different frequency to organize particles into complex, non-repeating patterns, which we call multi-frequency ultrasound DSA. We theoretically derive and experimentally validate a method that allows us to assemble any specific two-dimensional pattern of particles using multi-frequency ultrasound DSA. The results show that multi-frequency ultrasound DSA enables the assembly of complex, non-repeating patterns of particles with substantially resources than single-frequency ultrasound DSA, and without incurring a penalty in terms of accuracy. Multi-frequency ultrasound DSA enables a near-unlimited complexity of patterns of particles that can be assembled, increasing the relevance of the technology to practical implementation in engineering applications.

Dedication

I dedicate this Master's thesis to my Heavenly Father. You have blessed me with the opportunity to learn and receive an education. Through this blessing, I have grown deeper in my faith and learned to trust you even when it seems impossible. I am forever grateful that your love for your son overflows to humanity.

I dedicate this Master's thesis to my savior, Jesus Christ. Through your obedience to your Father, I am a new creation with new life and a co-heir, an adopted son of the living God. Through your love for your creation, I can have an intimate relationship with my Heavenly Father. In your death and resurrection, you left your Spirit with humanity that we may experience your presence.

I dedicate this Master's thesis to the Holy Spirit. You dwell within me and guide me. You give me new life, peace, and joy even in the hardest circumstances. You empower me to live out my faith and become a better follower of Christ, husband, and friend each day. Through you, I am bound to the Father and Son and experience the love that they share.

I dedicate this Master's thesis to my beautiful wife, Bailey. Your unwavering support throughout my educational journey means the world to me. I am so grateful to have you by my side and want to thank you for the love, support, and encouragement you have poured into me throughout this process. Thank you for being patient with me even when it is difficult, which is more often than not. Bailey, I love you and can never truly tell you all that you mean to me. I cannot wait to see what the Lord has in store for us.

Acknowledgement

Mom and Dad, you both have pushed me to achieve great things. Without your support, both emotional and financial, this would not be possible. I don't know that I'll ever be able to say how truly grateful I am for that. Thank you both for loving me unconditionally. I love you both so much.

JoJo and Keith, you have been in my life almost as long as you haven't. Thank you for always loving me like your son. Thank you for game nights, fishing trips, and home-cooked meals. I love you both and am grateful to have you in my life.

To my dearest friend, Soheyl, you have been listening ear when I needed it most. You have been a friend in my most trying times. I am so incredibly grateful for your friendship. I will miss annoying each other and all the small things, such as laughing together, drinking coffee, and talking about life, that make our friendship so enjoyable.

I want to thank both Dr. Bart Raeymaekers and Dr. Fernando Guevara Vasquez. Your mentorship and guidance means so much to me. You have both taught me what it means to be a researcher. I thank you for your support and encouragement throughout my research journey and am grateful to have had the opportunity to work with you both.

I am deeply grateful to the Department of Defense National Defense Science and Engineering Graduate fellowship foundation for their generous support that has allowed me to pursue my studies with dedication and focus.

I want to also acknowledge the Advanced Research Computing center at Virginia Tech for providing computational resources and technical support that have contributed to the results reported within this thesis.

Table of Contents

Abstract	ii
General Audience Abstract	iv
Dedication	v
Acknowledgement	vi
Table of Contents	vii
List of Figures	viii
List of Tables	ix
1. Significance of research	1
2. Introduction	3
3. Methods and materials	7
3.1. Theoretical model	7
3.2. Experimental validation	14
4. Results and discussion	18
5. Conclusions	29
References	31
Appendix	35

List of Figures

Figure 1. Engineered composite materials with tailored mechanical, thermal, optical, and electrical properties, showing (a) a dog-bone specimen with aligned bundles of carbon nanotubes (CNTs) [1] (b) a diamond polymer heat sink [2] (modified and reprinted with permission from The Royal Society of Chemistry), (c) an optical cloaking device [3] (modified and reprinted with permission from IEEE Transactions on Nanotechnology), and (d) an electrically conductive polymer matrix composite material [4].	2
Figure 2. Arbitrary-shaped, 2D fluid reservoir, lined with N_t ultrasound transducers along its boundary Ω . The boundary Ω comprises N_b boundary elements $d\epsilon(\mathbf{q})$ with normal vector $\mathbf{n}(\mathbf{q})$ at their center \mathbf{q} , and it encloses domain D , discretized with N_d domain points.	8
Figure 3. (a) Schematic and (b) photograph of the experimental setup with carbon microparticles (dark color) dispersed in water (light color), depicting four stacks of ultrasound transducers with $f_c = 1$ MHz (dark gray) and $f_c = 1.5$ MHz (light gray), one on each side of the square reservoir. When energizing single transducers (outlined in orange) to create a single-frequency ultrasound wave field, we observe the patterns of particles resulting from (c) the 1 MHz ultrasound transducers and (d) the 1.5 MHz ultrasound transducers.	14
Figure 4. Specific (center), simulated (left), and experimental (right) non-periodic patterns of particles produced by solving the inverse multi-frequency ultrasound DSA problem for specific patterns of particles, including (a) line patterns in the x -direction, (b) line patterns in the y -direction, and (c) dot patterns.	18
Figure 5. Specific pattern of particles X_d we aim to assemble (left) and theoretical (right) pattern of particles, showing (a) a square with a missing vertex, (b) a smiley face, and (c) the Virginia Tech “VT” logo.	23
Figure 6. SSIM as a function of the eigenvector subspace threshold τ for the three specific patterns of particles, including (a) a square with a missing vertex, (b) a smiley face, and (c) the Virginia Tech “VT” logo with inset images illustrating the theoretical pattern of particles for selected values of τ .	25
Figure 7. Specific pattern we aim to assemble (red) and theoretical pattern of particles showing the Virginia Tech “VT” logo using (a) single-frequency ultrasound DSA in a square reservoir with $N_t = 1,600$ ultrasound transducers and (b) multi-frequency ultrasound DSA in a square reservoir with $N_t = 16$ ultrasound transducers.	27

List of Tables

Table 1. v^* for selected results of multi-frequency ultrasound DSA	19
--	----

1. Significance of research

The ability to design and manufacture multi-functional composite materials with tailored properties, including optical, thermal, electrical, acoustic, and/or mechanical properties, is of interest to the scientific community because of its potentially game-changing impact on many engineering applications. Figure 1 shows several examples of such multi-functional composite materials that comprise filler embedded in a matrix material. The properties of the composite materials derive from the spatial arrangement of the filler (particles) in the matrix material, in addition to the properties of the filler and the matrix. The interactions between the particles and the matrix define the bulk properties of the composite material, and its response to an external field. Thus, changing the properties of the matrix and particles and the spatial organization and orientation of particles in the matrix allows modifying and tailoring the material properties of the composite material, which is an active research area.

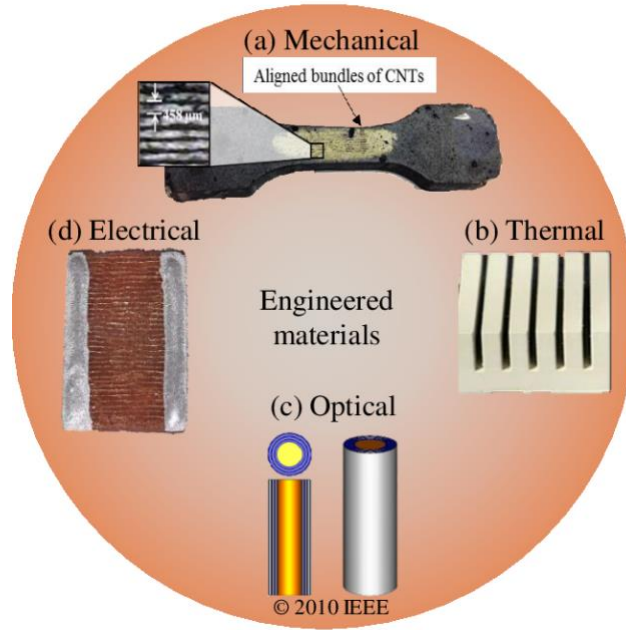


Figure 1. Engineered composite materials with tailored mechanical, thermal, optical, and electrical properties, showing (a) a dog-bone specimen with aligned bundles of carbon nanotubes (CNTs) [1] (b) a diamond polymer heat sink [2] (modified and reprinted with permission from The Royal Society of Chemistry), (c) an optical cloaking device [3] (modified and reprinted with permission from IEEE Transactions on Nanotechnology), and (d) an electrically conductive polymer matrix composite material [4].

Several methods exist to spatially arrange and/or orient (spherical and high-aspect-ratio) particles in a polymer matrix. Many of these methods rely on external field-driven directed self-assembly (DSA). For instance, electric and magnetic fields orient particles in the field direction but restrict material choice and require ultra-high field strengths, inhibiting the dimensional scalability of the specimens. On the other hand, ultrasound wave fields spatially arrange and orient particles, leveraging the acoustic radiation force (ARF) associated with a standing ultrasound wave, which exists independent of material properties or particle shape. Furthermore, ultrasound wave fields exhibit low attenuation in low-viscosity fluids, thus facilitating dimensional scalability. The literature documents successful examples of creating 1D, 2D, and 3D patterns of spherical and high-aspect-ratio

particles using ultrasound DSA based on a single-frequency wave field. However, the critical problem is that these implementations are limited to creating periodic patterns of particles (i.e., pattern spacing equal to a half-wavelength of the wave field), which restricts the achievable material designs. Thus, this proposal aims to use ultrasound DSA with multi-frequency wave fields to create user-specified, non-periodic patterns of particles dispersed in a matrix material.

The research objective of this thesis is to test the hypothesis that the acoustic radiation force resulting from a superposition of multiple standing ultrasound waves with different frequencies can assemble particles dispersed in a fluid medium into any user-specified, non-periodic patterns.

This research advances the state-of-the-art by considering the superposition of multiple ultrasound waves with different frequencies to create non-periodic patterns of particles compared to demonstrations with single-frequency wave fields used to create periodic patterns of particles. The ability to assemble particles into non-periodic patterns is useful for fabricating composite materials with designer properties. Ultrasound DSA works independently of material properties and, thus, does not restrict material choice. Furthermore, ultrasound waves show limited attenuation in viscous fluids, thus enabling dimensional scalability. Hence, this research allows, for the first time, the creation of non-periodic patterns of particles using standing ultrasound waves to fabricate composite materials with tailored properties. We follow a combined theoretical and experimental approach.

Most composite materials manufacturing methods are time-consuming, not easily scalable, and require expensive equipment. In contrast, ultrasound DSA relies on an

inexpensive bench-top setup, thus enabling a quick turnaround between material design and implementation. This research could revolutionize the design and fabrication of polymer composite materials with designer properties by enabling the creation of material specimens with embedded, non-periodic patterns of particles in an expeditious manner using ultrasound DSA.

2. Introduction

Directed self-assembly (DSA) is a process by which particles or other discrete components dispersed in a fluid medium organize as a result of interactions between the components themselves and/or with their environment [5]. External field DSA techniques employ a set of transducers to establish an electric [6], magnetic [7], or ultrasound wave [8] field, and the forces associated with the field organize and orient the particles into specific patterns. Modifying the operating parameters of the transducers changes the field which, in turn, tunes the organization and orientation of the particles. Electric [9] and magnetic [10] fields enable organizing and orienting (high-aspect ratio) particles, but they restrict material choice and require ultra-high field strengths [11,12] that limits dimensional scalability. Ultrasound DSA on the other hand, relies on the acoustic radiation force associated with a standing ultrasound wave field to organize and orient particles into specific patterns. The existence of the acoustic radiation force only depends on the acoustic contrast between the particles and the fluid medium, which derives from their density and compressibility [13]. Furthermore, dimensional scalability is limited only by the attenuation of the ultrasound wave in the fluid medium [14]. King began theoretical studies of the acoustic radiation force of incompressible spherical particles suspended in an inviscid fluid in the 1930s [15]. Subsequently, Yosioka and Kawasima considered

compressible spherical particles in an inviscid fluid to extend King’s analysis [16]. Finally, Gor’kov generalized earlier theories, and formulated an acoustic radiation force theory for compressible spherical particles, smaller than the acoustic wavelength, and dispersed in an inviscid fluid medium [17].

Ultrasound DSA reduces to a forward problem, which determines the organization and orientation of particles that result from a set of ultrasound transducers and their operating parameters (frequency, amplitude, and phase), and an inverse problem, in which we calculate the operating parameters of the set of ultrasound transducers, required to organize and orient particles into a specific pattern. The literature documents theoretical solutions to both the forward and inverse problems for spherical particles in one-dimension (1D) [18], two-dimensions (2D) [19–21], and three dimensions (3D) [22–24], as well as for high-aspect ratio particles in 2D [25] and 3D [26], mostly in inviscid media, even though some also show experimental validation in viscid media.

Settnes and Bruus [27] expanded Gor’kov’s acoustic radiation force theory from inviscid to viscous media. Using this viscous theory, Noparast et al. [28] illustrated that considering viscous as opposed to inviscid media in ultrasound DSA modifies the organization of particles because the sound propagation velocity changes with viscosity. Obtaining a fundamental understanding of ultrasound DSA in inviscid and viscous media has rendered it useful in engineering applications, e.g. to manufacture engineered composite materials with tailored properties [4,29–31], to manipulate and sort biological cells in lab-on-a-chip applications [32–35], to perform non-contact particle manipulation for acoustic displays [36–39], and to implement microbubble-aided drug delivery systems [40], amongst others applications.

However, existing theory and state-of-the-art experimental demonstrations are limited to assembling particles into (quasi-)periodic patterns, because they are based on single-frequency ultrasound wave fields (see e.g. [20,22,41–43]). Hence, the patterns of particles reflect the periodicity of the ultrasound wave field from which they originate and, consequently, single-frequency ultrasound wave fields limit the portfolio of patterns that can be assembled. Furthermore, the complexity of the patterns of particles that can be assembled generally increases with an increasing number of ultrasound transducers, because the superposition of different ultrasound wave fields creates increasingly complex ultrasound wave interference [20]. Even though theoretically possible, it is often practically difficult to increase the number of ultrasound transducers in experiments or physical applications due to manufacturing, alignment, and space constraints [20,22].

Alternative methods to assemble complex, non-periodic patterns of particles based on single-frequency ultrasound wave fields, have also been attempted, including acoustic holography, in which researchers spatially modulate the amplitude and/or phase of a single-frequency ultrasound wave field using a 3D-printed acoustic kinoform [44–47], microbubble arrays [48], or acoustic waveguides that direct acoustic energy into targeted regions [49,50]. These methods allow assembling particles in complex, non-periodic patterns, but generally display low spatial accuracy and require custom (often 3D printed) hardware for a limited number (see e.g. [51]), or even a single specific pattern of particles. Moreover, as a result of the custom hardware, they do not offer re-configurability, which is needed for many engineering applications. Hou et al. [52] show simulations of symmetric, complex patterns of particles, based on an indirect method that identifies resonance modes within a simulated reservoir filled with an inviscid liquid and particles.

However, the frequencies used are limited to the resonance modes of the reservoir and, moreover, they do not experimentally validate their method.

Hence, practical limitations to assemble complex, non-periodic patterns of particles have limited the adoption and impact of ultrasound DSA in engineering applications. However, the ability to assemble re-configurable, complex, non-periodic patterns of particles with a small number of ultrasound transducers would fundamentally change the practical applicability and relevance of ultrasound DSA in engineering applications, as it solves the two main shortcomings of the different state-of-the-art ultrasound DSA implementations, i.e., creating non-periodic patterns of unbound complexity and re-configurability.

Thus, the objective of this work is to implement ultrasound DSA using multi-frequency rather than single-frequency ultrasound wave fields. We theoretically derive a framework that relates any specific pattern of particles to any multi-frequency ultrasound wave field, generated by any spatial arrangement and number of ultrasound transducers, accounting for the properties of the particles, the fluid medium, and the ultrasound transducers. We use experiments to validate the theory, and expand the validation with simulations that demonstrate its capability to assemble complex, non-periodic, multi-dimensional patterns of particles. Although this work focuses on ultrasound DSA, the same principle could apply to other external field DSA.

3. Methods and materials

3.1. Theoretical model

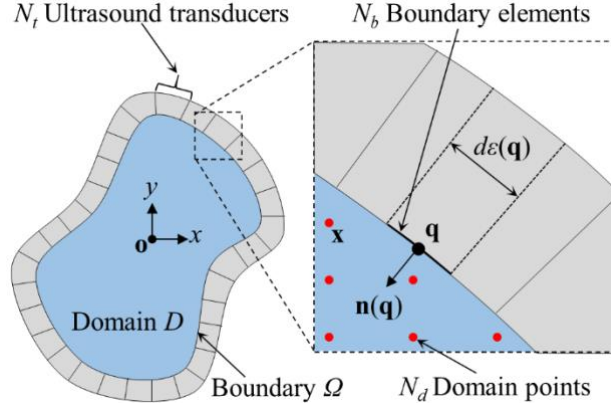


Figure 2. Arbitrary-shaped, 2D fluid reservoir, lined with N_t ultrasound transducers along its boundary Ω . The boundary Ω comprises N_b boundary elements $d\epsilon(\mathbf{q})$ with normal vector $\mathbf{n}(\mathbf{q})$ at their center \mathbf{q} , and it encloses domain D , discretized with N_d domain points.

Figure 2 schematically illustrates the theoretical model, which represents an arbitrary-shaped, 2D fluid reservoir lined with N_t ultrasound transducers along its perimeter. The ultrasound transducers act as ideal piston sources and emit a multi-frequency ultrasound wave field, which we discretize in $N_f = 64$ uniformly distributed frequencies between $150 \text{ kHz} \leq f_j \leq 6 \text{ MHz}$ based on practical considerations necessary to implement experiments, such as ultrasound wave attenuation, size of the fluid reservoir, and ultrasound transducer frequency range. The reservoir contains a fluid medium and compressible, spherical particles of radius $r_p \ll \lambda_s$, with λ_s the smallest wavelength of the multi-frequency ultrasound wave field. We discretize the boundary Ω of the reservoir using $N_b \geq N_t$ boundary elements $d\epsilon(\mathbf{q})$, with normal vector $\mathbf{n}(\mathbf{q})$ at their center point \mathbf{q} . The boundary Ω encloses the solution domain D , which we discretize using N_d domain points. We compute the ultrasound wave field with frequency f_j in terms of the time-independent,

complex scalar velocity potential φ_j . The velocity potential φ_j must satisfy (i) the Helmholtz equation $\nabla^2 \varphi_j + k_j^2 \varphi_j = 0$ in D , where $k_j = 2\pi f_j / c_m$ is the wavenumber of the ultrasound wave field of frequency f_j and c_m is the sound propagation velocity in the fluid medium, and (ii) the impedance boundary condition $\partial \varphi_j / \partial \mathbf{n} + ik_j Z \varphi_j = v_{jt}$ for all $t = 1, \dots, N_t$ ultrasound transducers on Ω . Here, $i = \sqrt{-1}$ and $Z = \rho_m c_m / Z_t$ is the impedance ratio of the fluid medium with density ρ_m and the ultrasound transducers, which captures the absorption and reflection of the ultrasound waves at the boundary Ω of the solution domain D . $v_{jt} = V_{jt} \exp(i\theta_{jt})$ for active ultrasound transducers, and V_{jt} and θ_{jt} are the amplitude and phase of ultrasound transducer t at frequency f_j . $v_{jt} = 0$ for an inactive ultrasound transducer, e.g. a section of the reservoir boundary without ultrasound transducers. We calculate the velocity potential φ_j using Green's third identity at all points \mathbf{x} in the solution domain for each frequency f_j of the multi-frequency ultrasound wave field as [53,54]

$$\varphi_j(\mathbf{x}) = \Phi(\mathbf{x}) \int_{\Omega} G_j(\mathbf{q}, \mathbf{x}) v(\mathbf{q}) d\varepsilon(\mathbf{q}) - \Phi(\mathbf{x}) \int_{\Omega} \left[ik_j Z G_j(\mathbf{q}, \mathbf{x}) + \frac{\partial G_j(\mathbf{q}, \mathbf{x})}{\partial \mathbf{n}(\mathbf{q})} \right] \varphi_j(\mathbf{q}) d\varepsilon(\mathbf{q}). \quad (1)$$

Here, $\Phi(\mathbf{x}) = 2$ when \mathbf{x} is on Ω and $\Phi(\mathbf{x}) = 1$ when \mathbf{x} is in D . $d\varepsilon(\mathbf{q})$ is the infinitesimally small surface integration element at \mathbf{q} on Ω . $v(\mathbf{q})$ is the complex harmonic velocity amplitude of the ultrasound transducer surface at \mathbf{q} , i.e. the right-hand side of the impedance boundary condition. $G_j(\mathbf{q}, \mathbf{x})$ is the Green's function that represents the free ultrasound wave field of frequency f_j , emitted by a point source in \mathbf{q} and evaluated in \mathbf{x} , and calculated as [53]

$$G_j(\mathbf{q}, \mathbf{x}) = -\frac{i}{4} H_0(k_j |\mathbf{q} - \mathbf{x}|). \quad (2)$$

H_0 is the 0th order Hankel function of the first kind and $|\mathbf{q} - \mathbf{x}|$ is the Euclidean distance between \mathbf{q} and \mathbf{x} .

We relate the locations where particles assemble to the operating parameters of the ultrasound transducers using the time-averaged acoustic radiation potential (ARP) $U_j(\mathbf{x})$ and the acoustic radiation force $\mathbf{F}_j(\mathbf{x}) = -\nabla U_j(\mathbf{x})$ associated with the velocity potential ϕ_j of frequency f_j , given as [17,55]

$$U_j(\mathbf{x}) = 2\pi r_p^3 \rho_m \left\{ \frac{1}{3} k_j^2 \left[1 - \left(\frac{\beta_p}{\beta_m} \right)^2 \right] \left\langle |\phi_j(\mathbf{x})|^2 \right\rangle - \left[\frac{\rho_p - \rho_m}{2\rho_p + \rho_m} \right] \left\langle |\nabla \phi_j(\mathbf{x})|^2 \right\rangle \right\}. \quad (3)$$

$\left\langle |\phi_j(\mathbf{x})|^2 \right\rangle$ is the mean square fluctuation of the complex scalar velocity potential ϕ_j averaged over one wave period $T = 1/f_j$, and $\beta_m = 1/(\rho_m c_m^2)$ and $\beta_p = 1/(\rho_p c_p^2)$ are the compressibility of the fluid medium and particle, respectively. ρ_p is the density and c_p is the sound propagation velocity of the particle.

We superimpose the contributions of all frequencies f_j of the multi-frequency ultrasound wave field into a single ARP, which still satisfies the Helmholtz equation because of linearity. Therefore, the time-averaged ARP $U(\mathbf{x})$ that considers a multi-frequency ultrasound wave field, evaluated at \mathbf{x} , is given as

$$U(\mathbf{x}) = \sum_{j=1}^{N_f} U_j(\mathbf{x}) = \sum_{j=1}^{N_f} a_j \left\langle |\phi_j(\mathbf{x})|^2 \right\rangle - b \left\langle |\nabla \phi_j(\mathbf{x})|^2 \right\rangle, \quad (4)$$

with constants a_j and b defined as

$$a_j = \frac{2}{3} \pi r_p^3 \rho_m k_j^2 \left[1 - \left(\frac{\beta_p}{\beta_m} \right)^2 \right] \text{ and} \quad (5)$$

$$b = 2\pi r_p^3 \rho_m \left[\frac{\rho_p - \rho_m}{2\rho_p + \rho_m} \right]. \quad (6)$$

We use the formulation of Greenhall et al. [20] to calculate $U_j(\mathbf{x})$ for each frequency f_j of the multi-frequency ultrasound wave field as

$$U_j(\mathbf{x}) = \mathbf{v}_j^H \mathbf{Q}_j(\mathbf{x}) \mathbf{v}_j. \quad (7)$$

Here, $\mathbf{v}_j = [v_{j1}, \dots, v_{jI}, \dots, v_{jN_I}]^T$ is a vector that contains the operating parameters v_{jI} for all N_I ultrasound transducers and frequency f_j , \mathbf{v}_j^H is the conjugate transpose of \mathbf{v}_j , and the Hermitian matrix $\mathbf{Q}_j(\mathbf{x})$ contains information regarding the velocity potential ϕ_j (see Eq. (1)) as discussed in detail by Greenhall et al. [20]. Hence, we compute the time-averaged ARP resulting from a multi-frequency ultrasound wave field as the sum of the ARPs for each individual frequency as summarized in the Appendix, i.e.,

$$U(\mathbf{x}) = \sum_{j=1}^{N_f} U_j(\mathbf{x}) = \mathbf{v}^H \mathbf{Q}(\mathbf{x}) \mathbf{v}, \quad (8)$$

where $\mathbf{v} = [\mathbf{v}_1, \dots, \mathbf{v}_{N_f}]^T$ and contains all vectors \mathbf{v}_j that describe the operating parameters of all ultrasound transducers for each frequency f_j . \mathbf{v}^H is the conjugate transpose of \mathbf{v} , and $\mathbf{Q}(\mathbf{x})$ is a block diagonal Hermitian matrix with $\mathbf{Q}_1(\mathbf{x}) \dots \mathbf{Q}_I(\mathbf{x}) \dots \mathbf{Q}_{N_f}(\mathbf{x})$ along its main diagonal.

Particles assemble at the stable points \mathbf{x}_s where the acoustic radiation force $\mathbf{F}(\mathbf{x}) = -\nabla U(\mathbf{x})$ approaches zero and $\mathbf{F}(\mathbf{x})$ points to \mathbf{x}_s in a neighborhood of \mathbf{x}_s , which also correspond to the local minima of the time-averaged ARP with respect to the reservoir coordinates \mathbf{x} . Thus, to assemble particles at specific locations $\mathbf{x}_d \in X_d$, we minimize the average ARP \bar{U} at all points \mathbf{x}_d . Rather than solving for the operating parameters of the ultrasound transducers \mathbf{v} , we solve for the ultrasound wave field parameters \mathbf{u} , i.e., amplitude and phase of each frequency f_j of the multi-frequency ultrasound wave field, since the relationship between \mathbf{v} and \mathbf{u} is not always known. We calculate \bar{U} as

$$\bar{U} = \mathbf{u}^H \bar{\mathbf{Q}}_c \mathbf{u}. \quad (9)$$

Here, $\mathbf{u} = [\mathbf{u}_1, \dots, \mathbf{u}_{N_f}]^T$ contains all vectors \mathbf{u}_j that describe the ultrasound wave field parameters for each frequency f_j .

$$\bar{\mathbf{Q}}_C = \mathbf{C}^H \bar{\mathbf{Q}} \mathbf{C}, \quad (10)$$

with $\bar{\mathbf{Q}}$ the average of all matrices $\mathbf{Q}(\mathbf{x}_d)$ for $\mathbf{x}_d \in X_d$, and \mathbf{C} is a matrix that relates the operating parameters of the ultrasound transducers \mathbf{v} to those of the ultrasound wave field \mathbf{u} , i.e. $\mathbf{u} = \mathbf{C}\mathbf{v}$, based on the impedance boundary condition.

Finally, we formulate a constrained quadratic optimization problem to compute the ultrasound wave parameters \mathbf{u}^* , required to assemble particles in a specific pattern X_d as

$$\min \bar{U}, \text{ subject to } |\mathbf{u}| = 1. \quad (11)$$

We constrain $|\mathbf{u}| = 1$, to represent the maximum harmonic velocity of the ultrasound transducer surface. The minimum eigenvalue of $\bar{\mathbf{Q}}_C$ (see Eq. (9)) and its corresponding eigenvector create the minimum average ARP \bar{U} at all locations $\mathbf{x}_d \in X_d$.

However, $\bar{\mathbf{Q}}_C$ is a block diagonal matrix that contains information about the velocity potential $\phi_j(\mathbf{x}_d)$ for $\mathbf{x}_d \in X_d$ of each frequency f_j of the multi-frequency ultrasound wave field. Hence, each eigenvector corresponds to a single frequency within the multi-frequency ultrasound wave field. Thus, only considering the eigenvector that corresponds to the smallest eigenvalue of $\bar{\mathbf{Q}}_C$ limits the resulting ultrasound wave field to a single frequency. To consider a multi-frequency wave field, we calculate an equal weight linear combination of multiple eigenvectors of $\bar{\mathbf{Q}}_C$ that are within a threshold τ of the smallest eigenvalue γ_{min} , i.e.,

$$\mathbf{u}_\tau = \sum_{\gamma \leq \gamma_{min} + \tau(\gamma_{max} - \gamma_{min})} \mathbf{u}_\gamma. \quad (12)$$

Here, \mathbf{u}_γ is the eigenvector with eigenvalue γ , γ_{max} and γ_{min} are the maximum and minimum eigenvalues after eigendecomposition, respectively, and τ is the eigenvector threshold. By construction (see Eq. (9)), \bar{U} is the average of the eigenvalues of $\bar{\mathbf{Q}}_C$ in the interval $[\gamma_{min}, \gamma_{min} + \tau(\gamma_{max} - \gamma_{min})]$. We use equal weights in \mathbf{u}_τ to lend equal importance to each frequency in the multi-frequency ultrasound wave field. Note that the phase of the eigenvectors does not matter when computing \bar{U} , if there is at most one eigenvector per frequency. Crucially, it does not affect the locations where particle assemble dictated by Eq. (4), under the same assumption. If there are multiple eigenvectors, it may be possible to carry out a secondary optimization, but this is left for future studies.

The number of eigenvectors in the linear combination of Eq. (12) increases with increasing τ and, consequently the time-averaged ARP varies with varying τ . The optimal eigenvector threshold τ^* is unique to each specific pattern of particles X_d . We determine τ^* to maximize the ratio of \bar{U} at all locations $\mathbf{x} \notin X_d$ and $\mathbf{x}_d \in X_d$. Thus, the equal weight linear combination \mathbf{u}_τ with τ^* yields the ultrasound wave parameters \mathbf{u}^* required to establish a multi-frequency ultrasound wave field to assemble particles in a specific pattern X_d .

3.2. Experimental validation

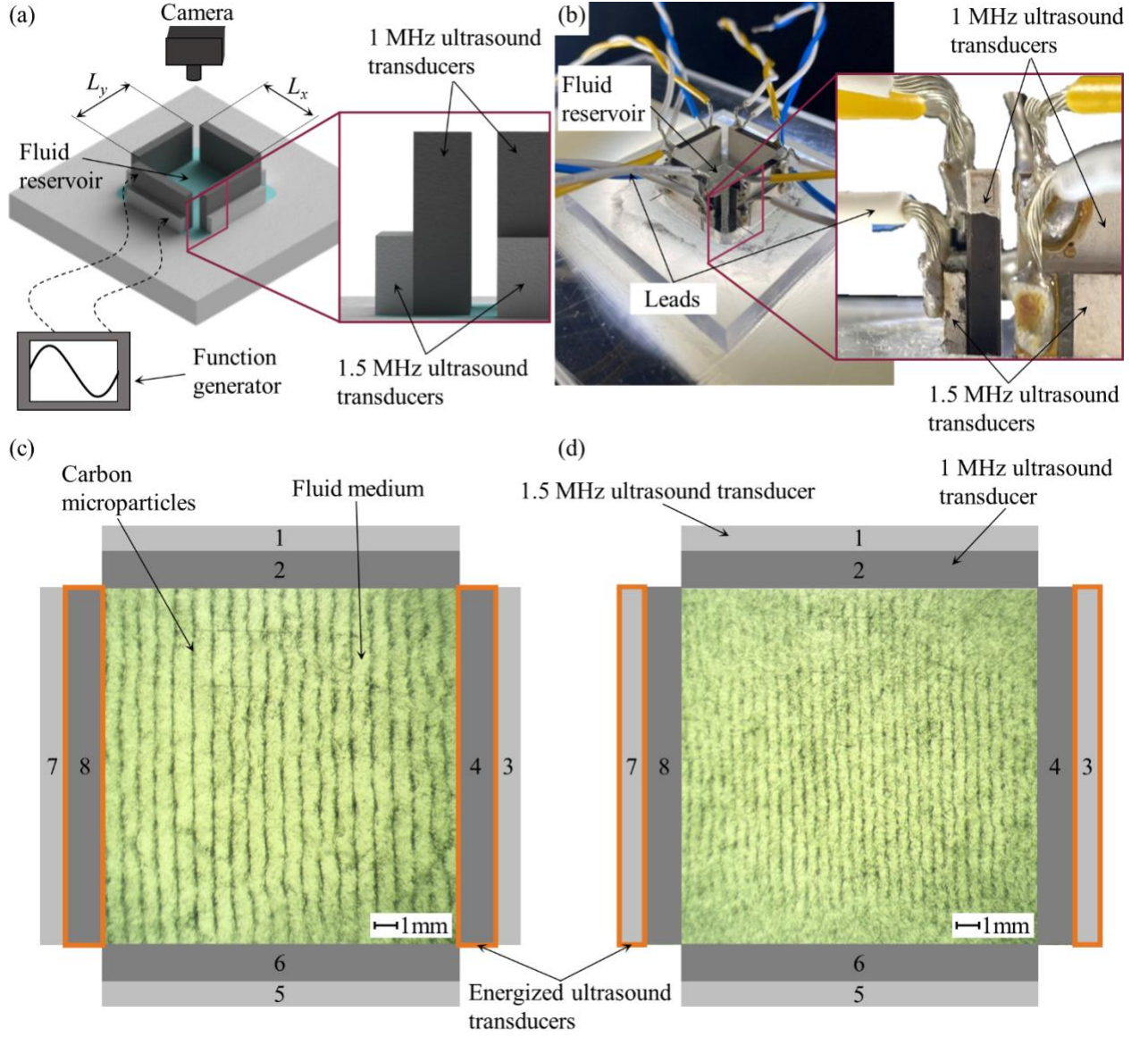


Figure 3. (a) Schematic and (b) photograph of the experimental setup with carbon microparticles (dark color) dispersed in water (light color), depicting four stacks of ultrasound transducers with $f_c = 1$ MHz (dark gray) and $f_c = 1.5$ MHz (light gray), one on each side of the square reservoir. When energizing single transducers (outlined in orange) to create a single-frequency ultrasound wave field, we observe the patterns of particles resulting from (c) the 1 MHz ultrasound transducers and (d) the 1.5 MHz ultrasound transducers.

Figure 3 shows the experimental set-up we use to validate the theoretical model, depicting a 3D schematic (Fig. 3 (a)), and a photograph (Fig. 3 (b)). The setup comprises

a square methyl methacrylate (plexiglass) reservoir with internal dimensions $L_x = L_y = 18$ mm, selected to balance the attenuation of the highest frequency and the near-field of the lowest frequency of the multi-frequency ultrasound wave field. The acrylic reservoir contains a mixture of water ($\rho_m = 998 \text{ kg}\cdot\text{m}^{-3}$, $c_m = 1482 \text{ m}\cdot\text{s}^{-1}$ [56]) and a 0.75% volume fraction of dispersed carbon microparticles (Zoltek PX30 MF150, $r_p = 3.6 \text{ }\mu\text{m}$, $\rho_p = 1750 \text{ kg}\cdot\text{m}^{-3}$, $c_m = 2000 \text{ m}\cdot\text{s}^{-1}$ [57]), under standard temperature and pressure. The combination of ultrasound transducers ($Z_t = 33 \text{ MPa}\cdot\text{s}\cdot\text{m}^{-1}$ [58]) and fluid medium create a hard acoustic boundary with $Z = 0.045$.

To perform ultrasound DSA experiments with multi-frequency ultrasound wave fields, we require ultrasound transducers with broad bandwidth and high power output, to create an acoustic radiation force of sufficient amplitude to displace particles dispersed in a fluid medium, and cover a wide spectrum of frequencies to increase the complexity of the portfolio of patterns we assemble. Many ultrasound transducers show broad bandwidth in combination with low power output, which limits the magnitude of the acoustic radiation force and, thus, the ability to drive particles into specific patterns. On the other hand, lead zirconate titanate (PZT) ultrasound transducers typically show high power output, which allows displacing particles dispersed in the fluid medium when the ultrasound transducer is energized with an operating frequency $f \approx f_c$, where f_c is the thickness-mode center frequency of the PZT material. However, PZT ultrasound transducers typically show a narrow bandwidth.

Hence, we design a stack of two PZT ultrasound transducers; one with $f_c = 1 \text{ MHz}$ (Steminc, Florida, USA), and another one with $f_c = 1.5 \text{ MHz}$ (American Piezo, Pennsylvania, USA), glued together with a thin layer of superglue (Loctite, Ohio, USA),

and mounted to each side of the square reservoir. The full-width half maximum of the ultrasound transducers spans 950 kHz – 1.2 MHz and 1.5 MHz – 1.7 MHz, respectively. Figures 3 (a) and (b) show magnified inset images that illustrate the design and construction of the PZT stack, using two different sizes of PZT plates with so-called wraparound electrodes to accommodate the soldering of leads. Furthermore, Fig. 3 (c) and (d) show carbon microparticles organized in line patterns by energizing a single pair of ultrasound transducers to create a single-frequency ultrasound wave field of 1 MHz (Fig. 3 (c)) and 1.5 MHz (Fig. 3 (d)). We select these two center frequencies to experimentally demonstrate ultrasound DSA of non-periodic patterns of particles using a multi-frequency ultrasound wave field. An arbitrary function generator (Tektronix AFG3102, Oregon, USA) energizes each ultrasound transducer, and supplies an arbitrary waveform that is the superposition of the single-frequency ultrasound waves at their respective amplitude and phase, which constitute the multi-frequency ultrasound wave field that results from solving the inverse multi-frequency ultrasound DSA problem (see Section 3.1).

We experimentally validate the theoretical model as follows. First, we define a specific, non-periodic pattern of particles X_d in a square reservoir lined with $N_t = 4$ stacks of ultrasound transducers ($f_1 = 1$ MHz and $f_2 = 1.5$ MHz) that contains water with dispersed carbon microfibers. Then, we calculate the ultrasound wave parameters \mathbf{u}^* required to assemble the specific pattern of particles X_d by solving the inverse multi-frequency ultrasound DSA problem and convert \mathbf{u}^* to the operating parameters of the stacks of ultrasound transducers \mathbf{v}^* . Subsequently, we apply \mathbf{v}^* to both the theoretical model and the experimental setup to obtain a theoretical prediction and experimental observation of the resulting pattern of particles. The local minima of the time-averaged ARP visualize the

simulated organization of particles in a specific pattern, whereas we use an optical microscope with a digital camera (80X magnification, AmScope, California, USA) to observe and record the experimental result.

We determine the average pattern error E_{pat} , similar to what others have used and described previously [20,22,23,59], to quantify the similarity between the experimental and theoretical results. The pattern error is the average distance between the centroids of the specific pattern of particles X_d we aim to assemble, and either the theoretical or experimentally obtained pattern of particles, normalized by the smallest nominal pattern spacing $\lambda_s/2$, which is half the wavelength of the highest frequency of the multi-frequency ultrasound wave field.

4. Results and discussion

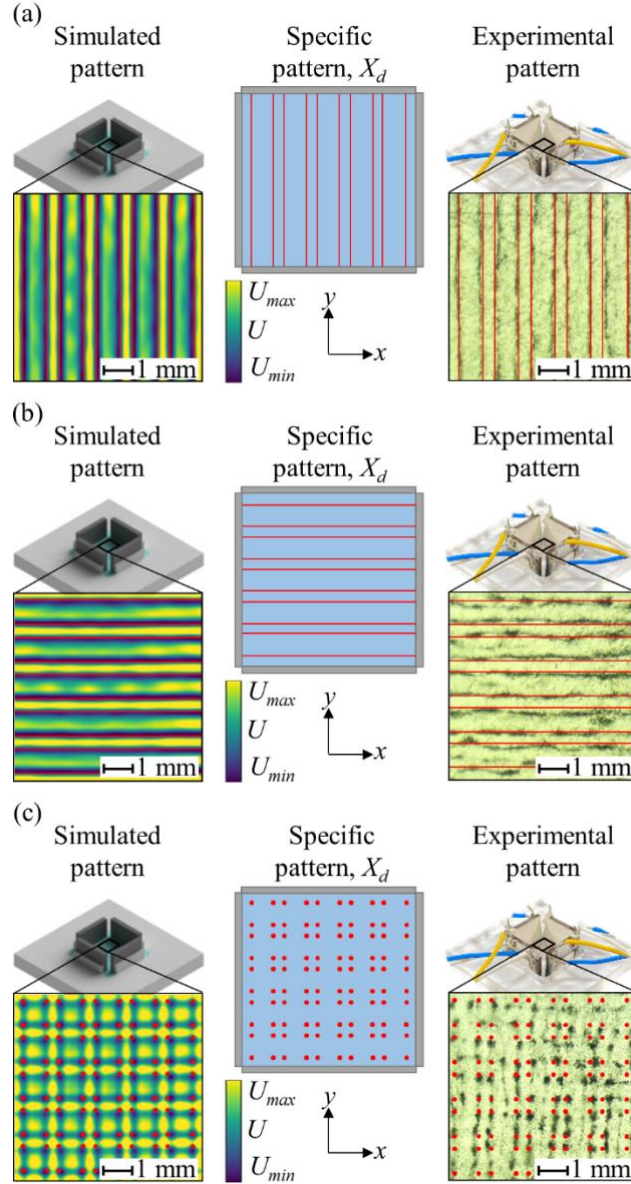


Figure 4. Specific (center), simulated (left), and experimental (right) non-periodic patterns of particles produced by solving the inverse multi-frequency ultrasound DSA problem for specific patterns of particles, including (a) line patterns in the x -direction, (b) line patterns in the y -direction, and (c) dot patterns.

Figure 4 shows three selected results that illustrate ultrasound DSA of non-periodic patterns of particles using multi-frequency ultrasound wave fields. Specifically, we demonstrate organizing non-periodic line patterns in the x -direction (Fig. 4 (a)), non-

periodic line patterns in the y -direction (Fig. 4 (b)), and dot patterns (Fig. 4 (c)). For each selected result, we depict a schematic of the specific pattern of particles X_d we aim to assemble (red lines), the theoretical results showing the time-averaged ARP of the multi-frequency ultrasound wave field (colormap, yellow: max, blue: min), and the experimental observations of particles (dark color) organized in non-periodic patterns in the fluid medium (light color), both resulting from solving the inverse ultrasound DSA problem and applying the results \mathbf{v}^* to the four stacks of ultrasound transducers (see Methods section). We summarize \mathbf{v}^* for each selected result of Fig. 4 (a), (b), and (c) in Table 1. We also superimpose the specific pattern of particles we aim to assemble (red solid lines/dots) on both the theoretical and experimental results, providing a qualitative assessment of the results.

Table 1. \mathbf{v}^* for each result of Fig. 3 with multi-frequency ultrasound DSA

Transducer	Frequency	Vertical lines	Horizontal lines	Dot pattern
1	f_2	0.00	$0.48\exp(2.87i)$	$0.32\exp(-2.86i)$
2	f_1	0.00	$0.56\exp(-2.63i)$	$0.38\exp(-2.86i)$
3	f_2	$0.47\exp(-2.97i)$	0.00	$0.31\exp(-2.82i)$
4	f_1	$0.54\exp(-2.64i)$	0.00	$0.38\exp(-3.02i)$
5	f_2	0.00	$0.45\exp(-3.06i)$	$0.36\exp(2.70i)$
6	f_1	0.00	$0.50\exp(2.78i)$	$0.36\exp(3.06i)$
7	f_2	$0.51\exp(2.79i)$	0.00	$0.35\exp(2.66i)$
8	f_1	$0.48\exp(2.79i)$	0.00	$0.38\exp(-3.06i)$

From Fig. 4 we qualitatively observe that multi-frequency ultrasound wave fields enable the assembly of non-periodic patterns of particles, which has never been shown before. Ultrasound DSA with single-frequency ultrasound wave fields cannot organize particles into non-periodic patterns. The three selected results of Fig. 4 also illustrate the underlying physics of ultrasound DSA with multi-frequency ultrasound wave fields. It is

intuitively evident that only two opposing stacks of ultrasound transducers are required to assemble the particles into non-periodic line patterns, whereas all four stacks are needed to assemble the non-periodic dot patterns, similar to single-frequency ultrasound wave fields [20,22].

From Fig. 4 (a), (b), and (c), we also determine the pattern error E_{pat} between the specific pattern of particles we aim to assemble, and the experimental and theoretical patterns of particles as $E_{pat} = 13.7\%$, 14.6% , and 15.9% , and $E_{pat} = 5.3\%$, 6.7% , and 6.0% , respectively. We note that the pattern error of the experimental pattern of particles is approximately double that of the theoretical pattern of particles. However, all pattern errors of the experimental patterns of particles are less than 16%, indicating good agreement between experiment and theory, and similar to pattern errors previously documented by our group for single-frequency ultrasound DSA (see e.g. [20,22]). Thus, multi-frequency ultrasound DSA does not appear to introduce a penalty in terms of accuracy compared to single-frequency ultrasound DSA.

The pattern error of the experiments results from imperfections, which include manufacturing tolerances of the acrylic reservoir that affect the alignment of the ultrasound transducers with respect to each other and the reservoir walls. Additionally, we create the stack of ultrasound transducers by manually gluing them together, which again introduces alignment error and a thin layer of glue, which acts as a soft spring between the two hard PZT plates. As a result, we measured slight variability of the center frequencies of the individual PZT plates in each stack. In contrast, the theoretical model assumes perfect reservoir geometry and alignment of the ultrasound transducers, and consistent center frequencies of the ultrasound transducers between different stacks. Furthermore, the

theoretical model assumes that the ultrasound transducers act as ideal piston sources, which is unlikely in the experiment as we must solder leads to the surfaces of the PZT plates, which locally adds mass and, thus, causes the transducers to deviate from the ideal piston source. We also note that even though we sonicate the mixture of water and carbon microparticles, their spatial distribution in the fluid medium is not perfectly uniform, even though the theoretical model considers that assumption. The pattern error of the theoretical pattern of particles results from the fundamental limitations of the theory, i.e., we limit the number of frequencies $N_f = 64$ in the multi-frequency ultrasound wave field, the number of boundary elements $N_b = 400$, and number of domain points $N_d = 10,000$ (spatial resolution $\sigma_x = L_x/100 = 0.18$ mm and $\sigma_y = L_y/100 = 0.18$ mm) for reason of computational cost. The theoretical model also only considers single scattering, even though because of the local close-packing of particles within the pattern features that result from ultrasound DSA, multiple scattering could improve accuracy [60], in addition to including secondary acoustic radiation forces [61]. Consequently, the imperfections introduced in the experiments explain why the pattern error of the theoretical compared to the experimental pattern of particles is substantially smaller.

The experiments show that it is increasingly difficult to align and independently control the frequency, amplitude, and phase of an increasing number of ultrasound transducers N_t , because of physically implementing the experiment, and the increasing instrumentation requirements. Therefore, we limit the experiments documented here to $N_t = 4$ stacks of two ultrasound transducers, which limits the complexity of the patterns of particles that we assemble using multi-frequency ultrasound DSA.

However, to illustrate the capability of the multi-frequency ultrasound DSA method in terms of organizing particles into complex, non-periodic patterns, we use simulations of the validated theoretical model within a square reservoir lined with $N_t = 16$ ultrasound transducers. Figure 5 shows three examples of using multi-frequency ultrasound DSA to organize complex patterns of particles; a square with a missing vertex (Fig. 5 (a)), a smiley face (Fig. 5 (b)), and the Virginia Tech “VT” logo (Fig. 5 (c)). Similar to Fig. 3, we depict the specific pattern of particles X_d we aim to assemble, and the time-averaged ARP (colormap, yellow: max, blue: min) of the theoretical pattern of particles. Particles assemble at the local minima of the ARP (dark blue locations).

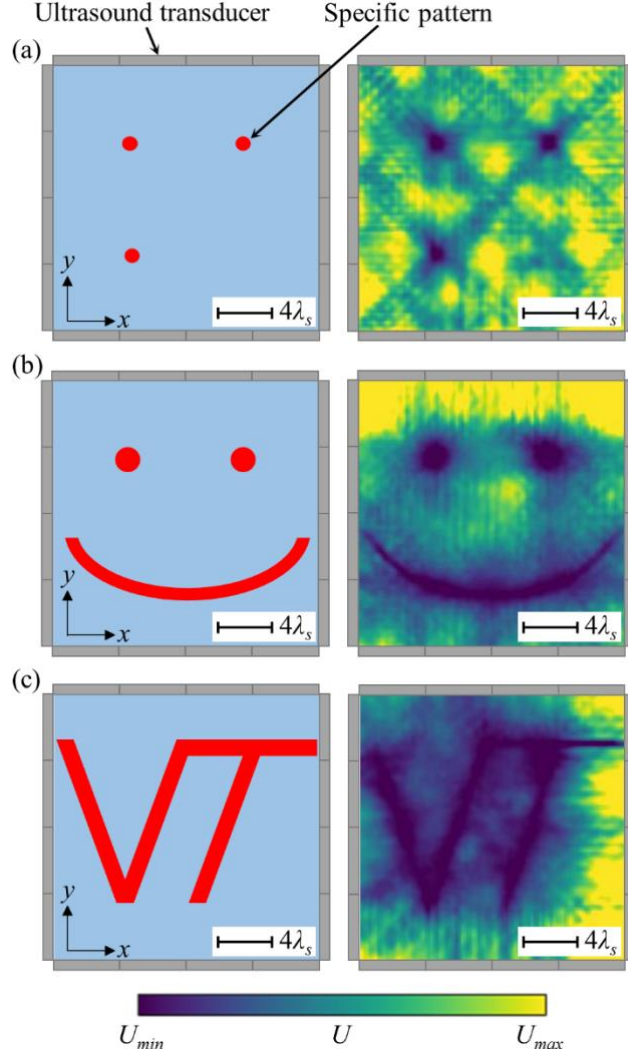


Figure 5. Specific pattern of particles X_d we aim to assemble (left) and theoretical (right) pattern of particles, showing (a) a square with a missing vertex, (b) a smiley face, and (c) the Virginia Tech “VT” logo.

From Fig. 5 we observe that multi-frequency ultrasound DSA enables organizing particles into complex patterns with a small number ($N_t = 16$) of ultrasound transducers. Furthermore, we qualitatively observe good agreement between each of the three specific patterns, and the corresponding theoretical results. We also quantitatively assess the similarity between the specific and theoretical patterns of particles by binarizing the time-averaged ARP, taking into account local color intensity variations using the adaptive

minimum binary threshold method [62,63], and defining the specific pattern of particles we aim to assemble as $\mathbf{x}_d \in X_d = 1$ and $\mathbf{x} \notin X_d = 0$. Then, we compare the binary images using the structural similarity index measure (SSIM), which quantitatively describes the similarity of two images by considering various aspects of human visual perception such as luminance and contrast [64]. We determine SSIM values of 0.94 (Fig. 5 (a)), 0.89 (Fig. 5 (b)), and 0.82 (Fig. 5 (c)), indicating good agreement (i.e., spatial accuracy) between the specific patterns of particles we aim to assemble and the theoretical patterns of particles obtained with the multi-frequency ultrasound DSA method.

We note in Section 3.1 that the optimal theoretical result depends on the eigenvector threshold τ , which defines the eigenvectors used in the equal weight linear combination \mathbf{u}_τ . Figure 6 (a), (b), and (c) show the SSIM as a function of τ for the three specific patterns of particles shown in Fig. 5 (a), (b), and (c), respectively, with inset images depicting the theoretical pattern for selected values of τ .

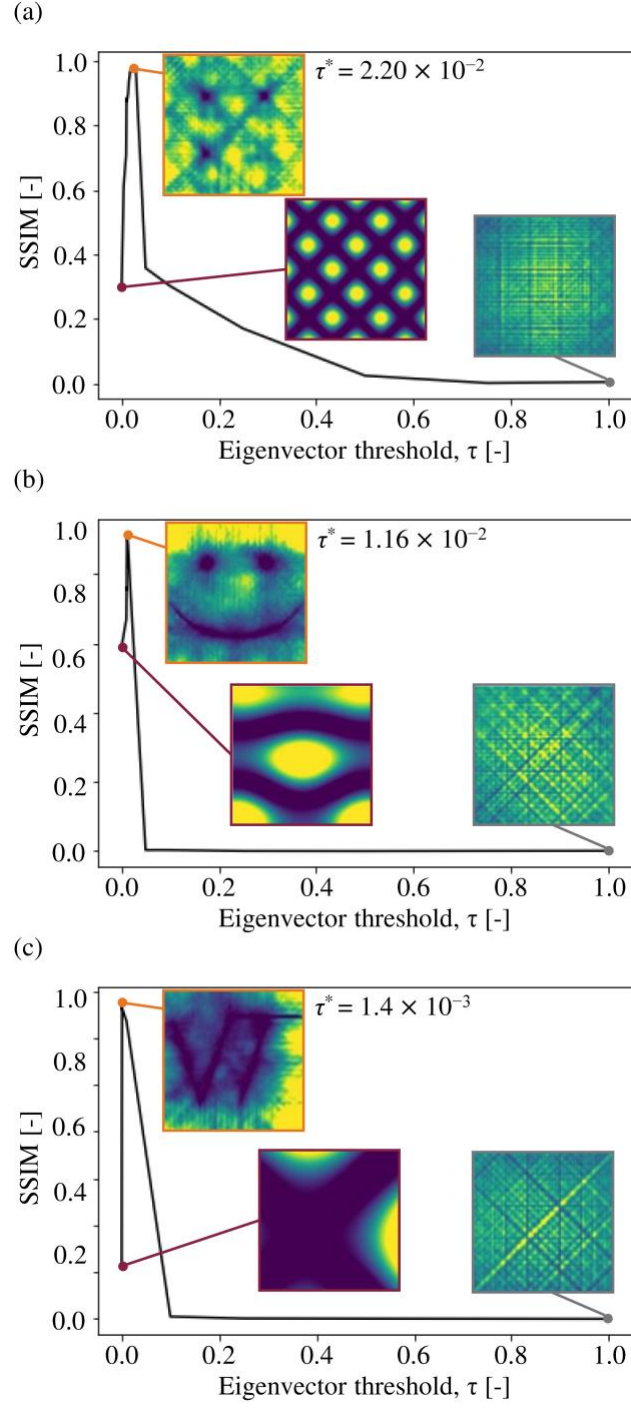


Figure 6. SSIM as a function of the eigenvector threshold τ for the three specific patterns of particles, including (a) a square with a missing vertex, (b) a smiley face, and (c) the Virginia Tech "VT" logo with inset images illustrating the theoretical pattern of particles for selected values of τ .

From Fig. 6, we observe that the maximum SSIM defines the optimal eigenvector subspace threshold τ^* and, correspondingly, the theoretical pattern of particles approaches the specific pattern X_d . The SSIM first increases and then decreases with increasing τ . The number of eigenvectors in the equal weight linear combination \mathbf{u}_τ increases with increasing τ , which in turn increases the number of frequencies included in the multi-frequency ultrasound wave field. Too few frequencies prevent local minima in the time-averaged ARP at all locations to assemble the specific pattern X_d , whereas too many frequencies establish additional local minima beyond those at the locations defined in X_d .

Finally, to illustrate the power of multi-frequency compared to single-frequency ultrasound DSA, we aim to assemble particles into the Virginia Tech “VT” logo pattern with both methods. Figure 7 shows the time-averaged ARP (colormap, yellow: max, blue: min) with the specific pattern superimposed (red). Particles assemble at the local minima of the time-averaged ARP (dark blue locations). Figure 7 (a) shows the theoretical pattern using single-frequency ultrasound DSA using $N_t = 1,600$ ultrasound transducers ($f = 1.5$ MHz), whereas Fig. 7 (b) shows the theoretical pattern using multi-frequency ultrasound DSA and only $N_t = 16$ ultrasound transducers ($150 \text{ kHz} \leq f_j \leq 6 \text{ MHz}$).

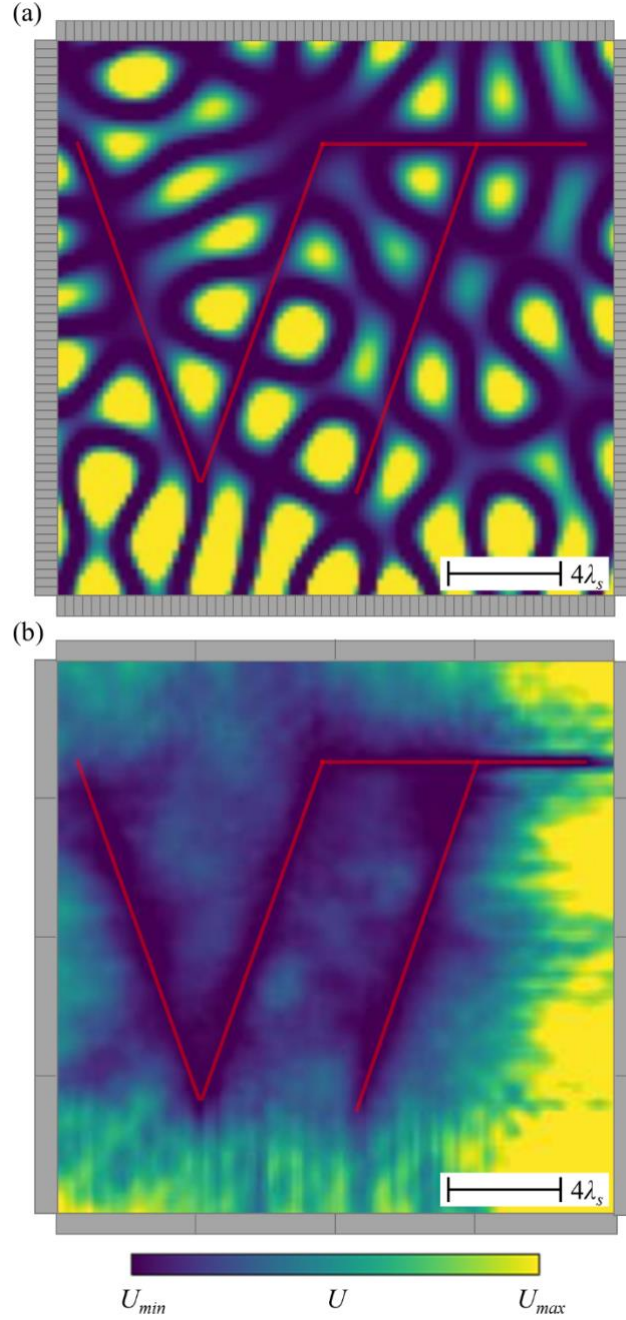


Figure 7. Specific pattern we aim to assemble (red) and theoretical pattern of particles showing the Virginia Tech “VT” logo using (a) single-frequency ultrasound DSA in a square reservoir with $N_t = 1,600$ ultrasound transducers and (b) multi-frequency ultrasound DSA in a square reservoir with $N_t = 16$ ultrasound transducers.

From Fig. 7 we qualitatively observe that the multi-frequency ultrasound DSA method approximates the Virginia Tech “VT” logo substantially better than the single-

frequency ultrasound DSA method. Evidently, the Virginia Tech “VT” logo is a non-periodic pattern and, thus, single-frequency ultrasound DSA is limited in approximating the pattern, even with a large number of ultrasound transducers. Furthermore, it is evident from Fig. 7 (a) that single-frequency ultrasound DSA would not actually result in the Virginia Tech “VT” logo, because there are many additional local minima in the time-averaged ARP that are not part of the Virginia Tech “VT” logo, but where particles will still assemble. In contrast, multi-frequency ultrasound DSA approximates the geometry of the Virginia Tech “VT” logo with remarkable accuracy using only 16 ultrasound transducers, owing to the ability to assemble non-periodic patterns of particles. We also quantify the $SSIM = 0.31$ (single-frequency ultrasound DSA) and $SSIM = 0.82$ (multi-frequency ultrasound DSA) for both results, confirming the qualitative observations.

The results of this work provide a framework that relates any specific pattern of particles to any multi-frequency ultrasound wave field, generated by any spatial arrangement and number of ultrasound transducers, accounting for the properties of the particles, the medium, and the ultrasound transducers and, thus, addresses the shortcomings of the state-of-the-art ultrasound DSA implementations, namely creating patterns of unbound complexity and re-configurability. This work advances the state-of-the-art in assembling complex, non-periodic patterns of particles and expands the impact of ultrasound DSA in engineering applications. Specifically, this work has implications for manufacturing engineered composite materials that derive their properties from the spatial organization of the filler in the matrix material as it broadens the portfolio of the patterns of particles that can be assembled using ultrasound DSA.

5. Conclusions

We present, for the first time, a solution to organizing particles in non-periodic patterns using periodic ultrasound waves. To accomplish this, we introduce multi-frequency ultrasound wave fields, and we derive a theoretical solution to the inverse multi-frequency ultrasound DSA problem for spherical, compressible particles dispersed in an inviscid fluid medium within an arbitrary-shaped, 2D reservoir lined with any number and spatial arrangement of ultrasound transducers. We also provide experimental validation. This theoretical solution determines the operating parameters (frequency, amplitude, and phase) of all ultrasound transducers, required to organize particles into any specific pattern. Based on the results of the experiments and simulations, we conclude the following:

1. The acoustic radiation forces associated with multi-frequency ultrasound wave fields enable the assembly of non-periodic patterns of particles, which is not possible with single-frequency ultrasound wave fields. Moreover, the accuracy of the assembly of specific patterns with multi-frequency ultrasound DSA is similar to that of single-frequency ultrasound DSA.
2. Multi-frequency ultrasound DSA enables the assembly of complex, 2D patterns of particles with substantially fewer ultrasound transducers than when using a single-frequency ultrasound wave field, if it is even possible to assemble the specific pattern with the latter method. The complexity of the patterns of particles that one can assemble increases with increasing number of ultrasound transducers, which is valid for both single- and multi-frequency ultrasound DSA, and with increasing number of frequencies in the multi-frequency ultrasound wave field.

3. Multi-frequency ultrasound DSA enables the assembly of complex patterns of particles with few unwanted pattern features, which starkly contrasts single-frequency ultrasound DSA, where unwanted pattern features are typically unavoidable since one is limited to assembling periodic patterns of particles.

The results of this work fundamentally transform the state-of-the-art knowledge of ultrasound DSA. Multi-frequency ultrasound wave fields provide a near-unlimited complexity of patterns of particles that can be assembled, increasing the relevance of the technology to practical implementation in engineering applications such as manufacturing of engineered composite materials that derive their properties from the spatial organization of the filler in the matrix material. Although this work focuses specifically on ultrasound wave fields, the theoretical model is valid for all wave phenomena.

References

- [1] Haslam, M. D., and Raeymaekers, B., 2014, "Aligning Carbon Nanotubes Using Bulk Acoustic Waves to Reinforce Polymer Composites," *Compos. Part B Eng.*, **60**, pp. 91–97.
- [2] Kalsoom, U., Peristyy, A., N. Nesterenko, P., and Paull, B., 2016, "A 3D Printable Diamond Polymer Composite: A Novel Material for Fabrication of Low Cost Thermally Conducting Devices," *RSC Adv.*, **6**(44), pp. 38140–38147.
- [3] Bilotti, F., Tricarico, S., and Vegni, L., 2010, "Plasmonic Metamaterial Cloaking at Optical Frequencies," *IEEE Trans. Nanotechnol.*, **9**(1), pp. 55–61.
- [4] Niendorf, K., and Raeymaekers, B., 2021, "Combining Ultrasound Directed Self-Assembly and Stereolithography to Fabricate Engineered Polymer Matrix Composite Materials with Anisotropic Electrical Conductivity," *Compos. Part B Eng.*, **223**, p. 109096.
- [5] Grzelczak, M., Vermant, J., Furst, E. M., and Liz-Marzán, L. M., 2010, "Directed Self-Assembly of Nanoparticles," *ACS Nano*, **4**(7), pp. 3591–3605.
- [6] Hermanson, K. D., Lumsdon, S. O., Williams, J. P., Kaler, E. W., and Velev, O. D., 2001, "Dielectrophoretic Assembly of Electrically Functional Microwires from Nanoparticle Suspensions," *Science*, **294**(5544), pp. 1082–1086.
- [7] Promislow, J. H. E., and Gast, A. P., 1996, "Magnetorheological Fluid Structure in a Pulsed Magnetic Field," *Langmuir*, **12**(17), pp. 4095–4102.
- [8] Lee, C., Lee, J., Lau, S. T., Zhou, Q., and Shung, K. K., 2010, "Single Microparticle Manipulation by an Ultrasound Microbeam," *2010 IEEE International Ultrasonics Symposium*, pp. 849–852.
- [9] Uk Jeon, H., Min Jin, H., Young Kim, J., Keun Cha, S., Ho Mun, J., Eun Lee, K., Jae Oh, J., Yun, T., Soo Kim, J., and Ouk Kim, S., 2017, "Electric Field Directed Self-Assembly of Block Copolymers for Rapid Formation of Large-Area Complex Nanopatterns," *Mol. Syst. Des. Eng.*, **2**(5), pp. 560–566.
- [10] Ye, L., Pearson, T., Dolbashian, C., Pstrak, P., Mohtasebzadeh, A. R., Fellows, B., Mefford, O. T., and Crawford, T. M., 2016, "Magnetic-Field-Directed Self-Assembly of Programmable Mesoscale Shapes," *Adv. Funct. Mater.*, **26**(22), pp. 3983–3989.
- [11] Kamat, P. V., Thomas, K. G., Barazzouk, S., Girishkumar, G., Vinodgopal, K., and Meisel, D., 2004, "Self-Assembled Linear Bundles of Single Wall Carbon Nanotubes and Their Alignment and Deposition as a Film in a Dc Field," *J. Am. Chem. Soc.*, **126**(34), pp. 10757–10762.
- [12] Fujiwara, M., Oki, E., Hamada, M., Tanimoto, Y., Mukouda, I., and Shimomura, Y., 2001, "Magnetic Orientation and Magnetic Properties of a Single Carbon Nanotube," *J. Phys. Chem. A*, **105**(18), pp. 4383–4386.
- [13] Chen, X., and Apfel, R. E., 1996, "Radiation Force on a Spherical Object in an Axisymmetric Wave Field and Its Application to the Calibration of High-Frequency Transducers," *J. Acoust. Soc. Am.*, **99**(2), pp. 713–724.
- [14] Kinsler, L. E., Frey, A. R., Coppens, A. B., and Sanders, J. V., 2000, *Fundamentals of Acoustics*, John Wiley & Sons.
- [15] King, L. V., 1934, "On the Acoustic Radiation Pressure on Spheres," *Proc. R. Soc. Lond. Ser. - Math. Phys. Sci.*, **147**(861), pp. 212–240.
- [16] Yosioka, K., and Kawasima, Y., 1955, "Acoustic Radiation Pressure on a Compressible Sphere," *Acta Acust. United Acust.*, **5**, pp. 167–173.

- [17] Gor'kov, L. P., 1962, "On the Forces Acting on a Small Particle in an Acoustical Field in an Ideal Fluid," *Sov. Phys. Dokl.*, **6**(9), pp. 773–775.
- [18] Greenhall, J., Guevara Vasquez, F., and Raeymaekers, B., 2013, "Continuous and Unconstrained Manipulation of Micro-Particles Using Phase-Control of Bulk Acoustic Waves," *Appl. Phys. Lett.*, **103**(7), p. 074103.
- [19] Bernassau, A. L., Courtney, C. R. P., Beeley, J., Drinkwater, B. W., and Cumming, D. R. S., 2013, "Interactive Manipulation of Microparticles in an Octagonal Sonotweezer," *Appl. Phys. Lett.*, **102**(16), p. 164101.
- [20] Greenhall, J., Guevara Vasquez, F., and Raeymaekers, B., 2016, "Ultrasound Directed Self-Assembly of User-Specified Patterns of Nanoparticles Dispersed in a Fluid Medium," *Appl. Phys. Lett.*, **108**(10), p. 103103.
- [21] Courtney, C. R. P., Ong, C.-K., Drinkwater, B. W., Bernassau, A. L., Wilcox, P. D., and Cumming, D. R. S., 2011, "Manipulation of Particles in Two Dimensions Using Phase Controllable Ultrasonic Standing Waves," *Proc. R. Soc. Math. Phys. Eng. Sci.*, **468**(2138), pp. 337–360.
- [22] Prisbrey, M., Greenhall, J., Guevara Vasquez, F., and Raeymaekers, B., 2017, "Ultrasound Directed Self-Assembly of Three-Dimensional User-Specified Patterns of Particles in a Fluid Medium," *J. Appl. Phys.*, **121**(1), p. 014302.
- [23] Prisbrey, M., and Raeymaekers, B., 2018, "Ultrasound Noncontact Particle Manipulation of Three-Dimensional Dynamic User-Specified Patterns of Particles in Air," *Phys. Rev. Appl.*, **10**(3), p. 034066.
- [24] Ochiai, Y., Hoshi, T., and Rekimoto, J., 2014, "Three-Dimensional Mid-Air Acoustic Manipulation by Ultrasonic Phased Arrays," *PLOS ONE*, **9**(5), p. e97590.
- [25] Prisbrey, M., and Raeymaekers, B., 2019, "Aligning High-Aspect-Ratio Particles in User-Specified Orientations with Ultrasound-Directed Self-Assembly," *Phys. Rev. Appl.*, **12**(1), p. 014014.
- [26] Prisbrey, M., Guevara Vasquez, F., and Raeymaekers, B., 2020, "Arranging Ellipsoidal Particles in Three-Dimensional User-Specified Orientations with Ultrasound-Directed Self-Assembly," *Phys. Rev. Appl.*, **14**(2), p. 024026.
- [27] Settnes, M., and Bruus, H., 2012, "Forces Acting on a Small Particle in an Acoustical Field in a Viscous Fluid," *Phys. Rev. E*, **85**(1), p. 016327.
- [28] Noparast, S., Guevara Vasquez, F., and Raeymaekers, B., 2022, "The Effect of Medium Viscosity and Particle Volume Fraction on Ultrasound Directed Self-Assembly of Spherical Microparticles," *J. Appl. Phys.*, **131**(13), p. 134901.
- [29] Li, X., Lim, K. M., and Zhai, W., 2022, "A Novel Class of Bioinspired Composite via Ultrasound-Assisted Directed Self-Assembly Digital Light 3D Printing," *Appl. Mater. Today*, **26**, p. 101388.
- [30] Scholz, M.-S., Drinkwater, B. W., and Trask, R. S., 2014, "Ultrasonic Assembly of Anisotropic Short Fibre Reinforced Composites," *Ultrasonics*, **54**(4), pp. 1015–1019.
- [31] Wadsworth, P., Nelson, I., Porter, D. L., Raeymaekers, B., and Naleway, S. E., 2020, "Manufacturing Bioinspired Flexible Materials Using Ultrasound Directed Self-Assembly and 3D Printing," *Mater. Des.*, **185**, p. 108243.
- [32] Mulvana, H., Cochran, S., and Hill, M., 2013, "Ultrasound Assisted Particle and Cell Manipulation On-Chip," *Adv. Drug Deliv. Rev.*, **65**(11), pp. 1600–1610.
- [33] Laurell, T., Petersson, F., and Nilsson, A., 2007, "Chip Integrated Strategies for Acoustic Separation and Manipulation of Cells and Particles," *Chem. Soc. Rev.*, **36**(3), pp. 492–506.

- [34] Johansson, L., Nikolajeff, F., Johansson, S., and Thorslund, S., 2009, “On-Chip Fluorescence-Activated Cell Sorting by an Integrated Miniaturized Ultrasonic Transducer,” *Anal. Chem.*, **81**(13), pp. 5188–5196.
- [35] Deok-Ho Kim, Haake, A., Yu Sun, Neild, A. P., Ihm, J.-E., Dual, J., Hubbell, J. A., Byeong-Kwon Ju, and Nelson, B. J., 2004, “High-Throughput Cell Manipulation Using Ultrasound Fields,” *The 26th Annual International Conference of the IEEE Engineering in Medicine and Biology Society*, IEEE, San Francisco, CA, USA, pp. 2571–2574.
- [36] Kozuka, T., Yasui, K., Tuziuti, T., Towata, A., and Iida, Y., 2007, “Noncontact Acoustic Manipulation in Air,” *Jpn. J. Appl. Phys.*, **46**(7B), pp. 4948–4950.
- [37] Hoshi, T., Ochiai, Y., and Rekimoto, J., 2014, “Three-Dimensional Noncontact Manipulation by Opposite Ultrasonic Phased Arrays,” *Jpn. J. Appl. Phys.*, **53**(7S), p. 07KE07.
- [38] Hirayama, R., Martinez Plasencia, D., Masuda, N., and Subramanian, S., 2019, “A Volumetric Display for Visual, Tactile and Audio Presentation Using Acoustic Trapping,” *Nature*, **575**(7782), pp. 320–323.
- [39] Marzo, A., Seah, S. A., Drinkwater, B. W., Sahoo, D. R., Long, B., and Subramanian, S., 2015, “Holographic Acoustic Elements for Manipulation of Levitated Objects,” *Nat. Commun.*, **6**(1), p. 8661.
- [40] Yamakoshi, Y., Nakajima, N., and Miwa, T., 2007, “Microbubble Trapping by Nonlinear Bubble Oscillation Using Pumping Wave,” *Jpn. J. Appl. Phys.*, **46**(7S), p. 4847.
- [41] Raeymaekers, B., Pantea, C., and Sinha, D. N., 2011, “Manipulation of Diamond Nanoparticles Using Bulk Acoustic Waves,” *J. Appl. Phys.*, **109**(1), p. 014317.
- [42] Courtney, C. R. P., Ong, C.-K., Drinkwater, B. W., and Wilcox, P. D., 2011, “Manipulation of Microparticles in Two Dimensions Using Counter-Propagating Ultrasonic Waves,” *2011 IEEE International Ultrasonics Symposium*, IEEE, Orlando, FL, USA, pp. 192–195.
- [43] Scholz, M.-S., Drinkwater, B. W., Llewellyn-Jones, T. M., and Trask, R. S., 2015, “Counterpropagating Wave Acoustic Particle Manipulation Device for the Effective Manufacture of Composite Materials,” *IEEE Trans. Ultrason. Ferroelectr. Freq. Control*, **62**(10), pp. 1845–1855.
- [44] Melde, K., Mark, A. G., Qiu, T., and Fischer, P., 2016, “Holograms for Acoustics,” *Nature*, **537**(7621), pp. 518–522.
- [45] Melde, K., Choi, E., Wu, Z., Palagi, S., Qiu, T., and Fischer, P., 2018, “Acoustic Fabrication via the Assembly and Fusion of Particles,” *Adv. Mater.*, **30**(3), p. 1704507.
- [46] Ma, Z., Holle, A. W., Melde, K., Qiu, T., Poeppel, K., Kadiri, V. M., and Fischer, P., 2020, “Acoustic Holographic Cell Patterning in a Biocompatible Hydrogel,” *Adv. Mater.*, **32**(4), p. 1904181.
- [47] Gu, Y., Chen, C., Rufo, J., Shen, C., Wang, Z., Huang, P.-H., Fu, H., Zhang, P., Cummer, S. A., Tian, Z., and Huang, T. J., 2020, “Acoustofluidic Holography for Micro- to Nanoscale Particle Manipulation,” *ACS Nano*, **14**(11), pp. 14635–14645.
- [48] Ma, Z., Melde, K., Athanassiadis, A. G., Schau, M., Richter, H., Qiu, T., and Fischer, P., 2020, “Spatial Ultrasound Modulation by Digitally Controlling Microbubble Arrays,” *Nat. Commun.*, **11**(1), p. 4537.
- [49] Bian, Y., Guo, F., Yang, S., Mao, Z., Bachman, H., Tang, S.-Y., Ren, L., Zhang, B., Gong, J., Guo, X., and Huang, T. J., 2017, “Acoustofluidic Waveguides for Localized Control of Acoustic Wavefront in Microfluidics,” *Microfluid. Nanofluidics*, **21**(8), p. 132.

- [50] Tung, K.-W., Chung, P.-S., Wu, C., Man, T., Tiwari, S., Wu, B., Chou, Y.-F., Yang, F., and Chiou, P.-Y., 2019, “Deep, Sub-Wavelength Acoustic Patterning of Complex and Non-Periodic Shapes on Soft Membranes Supported by Air Cavities,” *Lab. Chip*, **19**(21), pp. 3714–3725.
- [51] Brown, M. D., Cox, B. T., and Treeby, B. E., 2017, “Design of Multi-Frequency Acoustic Kinoforms,” *Appl. Phys. Lett.*, **111**(24), p. 244101.
- [52] Hou, Z., Li, J., Zhou, Z., and Pei, Y., 2022, “Programmable Particles Patterning by Multifrequency Excitation Radiation Force of Acoustic Resonance Modes,” *Int. J. Mech. Sci.*, **222**, p. 107232.
- [53] Wrobel, L. C., 2002, *The Boundary Element Method, Volume 1: Applications in Thermo-Fluids and Acoustics*, John Wiley & Sons.
- [54] Chandler-Wilde, S., and Langdon, S., 2007, “Boundary Element Methods for Acoustics.”
- [55] Barmatz, M., and Collas, P., 1985, “Acoustic Radiation Potential on a Sphere in Plane, Cylindrical, and Spherical Standing Wave Fields,” *J. Acoust. Soc. Am.*, **77**(3), pp. 928–945.
- [56] Haynes, W. M., Lide, D. R., and Bruno, T. J., 2014, *CRC Handbook of Chemistry and Physics*, CRC Press, Boca Raton.
- [57] Zhernokletov, D. M., Milyavskiy, V. V., Khishchenko, K. V., Charakhchyan, A. A., Borodina, T. I., Val’yano, G. E., Zhuk, A. Z., Elert, M., Furnish, M. D., Chau, R., Holmes, N., and Nguyen, J., 2008, “Shock-Wave Loading of Graphite in Steel Targets with Conic Cavities,” *Waikoloa (Hawaii)*, pp. 216–219.
- [58] Wang, Y., Tao, J., Guo, F., Li, S., Huang, X., Dong, J., and Cao, W., 2018, “Magnesium Alloy Matching Layer for High-Performance Transducer Applications,” *Sensors*, **18**(12), p. 4424.
- [59] Prisbrey, M., Guevara Vasquez, F., and Raeymaekers, B., 2020, “3D Ultrasound Directed Self-Assembly of High Aspect Ratio Particles: On the Relationship between the Number of Transducers and Their Spatial Arrangement,” *Appl. Phys. Lett.*, **117**(11), p. 111904.
- [60] Zhang, S., Qiu, C., Wang, M., Ke, M., and Liu, Z., 2016, “Acoustically Mediated Long-Range Interaction among Multiple Spherical Particles Exposed to a Plane Standing Wave,” *New J. Phys.*, **18**(11), p. 113034.
- [61] Bjerknes, V. F. K., 1906, *Fields of Force: A Course of Lectures in Mathematical Physics Delivered December 1 to 23, 1905*, Columbia University Press, New York.
- [62] Prewitt, J. M., and Mendelsohn, M. L., 1966, “The Analysis of Cell Images,” *Ann. N. Y. Acad. Sci.*, **128**(3), pp. 1035–1053.
- [63] Glasbey, C. A., 1993, “An Analysis of Histogram-Based Thresholding Algorithms,” *CVGIP Graph. Models Image Process.*, **55**(6), pp. 532–537.
- [64] Wang, Z., Bovik, A. C., Sheikh, H. R., and Simoncelli, E. P., 2004, “Image Quality Assessment: From Error Visibility to Structural Similarity,” *IEEE Trans. Image Process.*, **13**(4), pp. 600–612.

Appendix

Derivation of the transition from Eq. (7) to Eq. (8) (see Section 3.1)

Section 3.1 indicates that the scalar velocity potential ϕ_j must satisfy the Helmholtz equation $\nabla^2 \phi_j + k_j^2 \phi_j = 0$ in the solution domain D and on the boundary Ω for all distinct frequencies f_j , where $j = 1, \dots, N_f$ and $k_j = 2\pi f_j / c_m$ is the wavenumber of the ultrasound wave field in the fluid medium with sound propagation velocity c_m .

The solutions ϕ_j to the Helmholtz equation correspond to the time harmonic functions

$$\phi_j(x, t) = \phi_j(x) e^{-i2\pi f_j t} \quad (\text{S1})$$

The multi-frequency ultrasound wave field in the time domain is given by the superposition of the ultrasound wave field of all frequencies f_j , i.e.,

$$\phi(x, t) = \sum_{j=1}^{N_f} \phi_j(x, t) \quad (\text{S2})$$

Our goal in this section is to show that:

$$\langle |\phi(x, t)|^2 \rangle = \sum_{j=1}^{N_f} |\phi_j(x)|^2 \quad \text{and} \quad (\text{S3})$$

$$\langle |\nabla \phi(x, t)|^2 \rangle = \sum_{j=1}^{N_f} |\nabla \phi_j(x)|^2. \quad (\text{S4})$$

In Eq. (8) (see manuscript), we define the time-averaged acoustic radiation potential (ARP) of the multi-frequency wave field $U(\mathbf{x})$ at \mathbf{x} as the summation of the time-averaged ARP U_j for all single-frequency ultrasound wave fields. From the construction in Eq. (4) (see manuscript), the mean-square fluctuations in the time-domain are calculated as

$$\langle |\phi(x, t)|^2 \rangle = \lim_{T \rightarrow \infty} \frac{1}{T} \int_0^T |\phi(x, t)|^2 dt \quad \text{and}$$

(S5)

$$\langle |\nabla \phi(x, t)|^2 \rangle = \lim_{T \rightarrow \infty} \frac{1}{T} \int_0^T |\nabla \phi(x, t)|^2 dt. \quad (\text{S6})$$

From Eq. (S5), we observe that

$$\frac{1}{T} \int_0^T |\phi(x, t)|^2 dt = \frac{1}{T} \int_0^T \left| \sum_{j=1}^{N_f} \phi_j(x, t) \right|^2 dt = \frac{1}{T} \int_0^T \sum_{j=1}^{N_f} \sum_{j'=1}^{N_f} \bar{\phi}_j(x, t) \phi_{j'}(x, t) dt. \quad (\text{S7})$$

When $j = j'$, Eq. (S7) reduces to

$$\frac{1}{T} \int_0^T |\phi_j(x, t)|^2 dt = \frac{1}{T} \int_0^T |\phi_j(x)|^2 dt = |\phi_j(x)|^2. \quad (\text{S8})$$

When $j \neq j'$, Eq. (S7) becomes

$$\begin{aligned} \frac{1}{T} \sum_{j=1}^{N_f} \sum_{j'=1}^{N_f} \int_0^T \bar{\phi}_j(x, t) \phi_{j'}(x, t) dt &= \lim_{T \rightarrow \infty} \frac{1}{T} \sum_{j=1}^{N_f} \sum_{j'=1}^{N_f} \int_0^T \bar{\phi}_j(x) \phi_{j'}(x) e^{-i2\pi(f_j - f_{j'})t} dt \dots \\ &= \frac{1}{T} \sum_{j=1}^{N_f} \sum_{j'=1}^{N_f} \bar{\phi}_j(x) \phi_{j'}(x) \int_0^T e^{-i2\pi(f_j - f_{j'})t} dt \dots \end{aligned}$$

$$\dots = \frac{1}{T} \sum_{j=1}^{N_f} \sum_{j'=1}^{N_f} \bar{\varphi}_j(x) \varphi_{j'}(x) \left[\frac{e^{-i2\pi(f_j - f_{j'})t}}{-i2\pi(f_j - f_{j'})} \right]_0^T. \quad (\text{S9})$$

Eq. (S9) approaches 0 when $T \rightarrow \infty$. The same principle applies to Eq. (S6). Thus, the statements of (S3) and (S4) hold.